Hindawi
Geofluids
Volume 2022, Article ID 9744086, 17 pages
https://doi.org/10.1155/2022/9744086

Research Article

Quantitative Characterization of Full-Spectrum Pore Size and Connectivity for Shale with Different Sedimentary Facies from the Dongying Depression, Bohai Bay Basin, East China

Yushan Du,[1] Na Yin,[2,3] Qinhong Hu,[4] Mianmo Meng,[5] Xiuchuan Zhu,[2] Jing Chao,[1] and Cunfei Ma[2]

[1]*Exploration and Production Research Institute of Shengli Oilfield Company, Sinopec, Dongying, Shandong 257015, China*
[2]*Shandong Provincial Key Laboratory of Deep Oil and Gas, China University of Petroleum (East China), Qingdao 266580, China*
[3]*Pilot National Laboratory for Marine Science and Technology (Qingdao), Qingdao 266071, China*
[4]*Department of Earth and Environmental Sciences, The University of Texas at Arlington, Texas 76019, USA*
[5]*Hubei Key Laboratory of Marine Geological Resources, China University of Geosciences, Wuhan 430074, China*

Correspondence should be addressed to Na Yin; 18306422290@163.com and Qinhong Hu; maxhu@uta.edu

Received 9 March 2022; Revised 24 April 2022; Accepted 25 April 2022; Published 31 May 2022

Academic Editor: Bailu Teng

Working with shales in the fourth member of Shahejie Formation in the Dongying Depression in Bohai Bay Basin of East China, this study examines the facies classification, petrological characteristics, pore size distribution, and pore connectivity of oil-producing shale. The studied shales could be classified into five sedimentary facies according to a three-step classification criterion that consists of total organic carbon (TOC), sedimentary structure, and mineral composition. Among them, the "low TOC massive siliceous mudstone" and "low TOC layered clayey mudstone" facies have similar distributions from low-pressure N_2 physisorption, and the incremental volume within the 3-30 nm pore size range is much higher than the "high TOC laminated clayey marlstone" and "low TOC layered siliceous marlstone" facies. The T_2 spectra of nuclear magnetic resonance tests for the "high TOC laminated clayey marlstone" facies which contains abundant calcite laminae and organic matter-hosted pores commonly show three peaks, with a dominant peak at less than 300 nm in diameter and good pore connectivity. The T_2 spectra of three other facies are both characterized by two peaks, and the main peak of the "low TOC layered siliceous marlstone" and "low TOC layered clayey mudstone" facies has a similar range at 2-500 nm, in contrast with 1-17 nm for the "low TOC massive siliceous mudstone" facies. Pores in these four facies are mainly at nanoscales with predominant pore-throat diameters at less than 50 nm; however, the "high TOC laminated clayey marlstone" facies has the largest peak in the range of >1 μm, possibly because of its interlaminar structure and microcracks. The spontaneous imbibition experiments using two distinct fluids indicated that all of four facies have a much better pore connectivity towards the hydrophilic fluid than these experienced by the hydrophobic fluid.

1. Introduction

With the continuously increasing demand for energy and the decline of conventional oil and gas production in the world, shale oil has become a focus of oil exploration [1–6]. Shale oil refers to oil that is contained in fine-grained shale formations with abundant organic matter and is preserved in mud, shale, and adjacent thin interlayers of sandstone and carbonate rocks [7–9]. Shale serves as not only a hydrocarbon source rock but also reservoir, and the micro-nano-scaled pores are the main reservoir space of shale oil, with their connectivity very important in understanding the occurrence state and migration capacity of shale oil [10, 11] and therefore attracting a widespread attention [12–15].

The experimental methods for full-spectrum nm-μm pore size distribution analyses are importantly required to produce representative and consistent results. Currently,

the main techniques for studying the pore structure of shale oil reservoirs include radiation detection methods (scanning electron microscopy (FE-SEM), nano-CT, X-ray diffraction (XRD), and small-angle/ultrasmall angle neutron scattering (SANS/USANS)) and fluid injection type (nuclear magnetic resonance (NMR), low-pressure N_2 physisorption (LNP), and mercury intrusion porosimetry (MIP) [16–18]. Because of the multiscale pore size distribution of shale and variable resolution limitation of each experimental technique, it is necessary to combine the advantages of each method to investigate the full-spectrum pore distribution and determine the pore connectivity of shales [19, 20]. Meanwhile, shales are fine-grained sedimentary rocks with a wide range of lithologies, and the study of complex lithological controls on shale oil accumulation and movement is critical for different lithofacies and facies [21–23]. Thus, the representativeness of experimental samples and methodologies for different facies was the key to successful research of shale oil exploration and production [24].

Based on various analyses and experiments of XRD, Rock-Eval, total organic carbon (TOC), FE-SEM, LNP, NMR, MIP, and spontaneous imbibition (SI), the main aims of this work are to (1) evaluate the pore structure characteristics using FE-SEM, LNP, NMR, and NMR cryoporometry (NMR_C) experiments; (2) assess the pore connectivity of shale using MIP and SI experiments; and (3) identify the relationship between different minerals and pore structure. Overall, these integrated tests on Shahejie Formation shale in Bohai Bay Basin will provide valuable information for pore structure characteristics and shale oil exploration in East China.

2. Samples and Experiments

2.1. Samples. A total of 13 shale samples from Shahejie Formation in Dongying Depression, Bohai Bay Basin, China (Figures 1 and 2), were collected, which was formed in a deep and semideep lake facies sedimentary environment [25]. For all samples, we have conducted the analyses of TOC, pyrolysis, XRD, and thin-section observations for comprehensive analyses of petrology and organic geochemistry. According to organic matter abundance, mineral composition, and sedimentary structure, the facies was divided for these shale samples (Figure 3; [26]). Afterward, four typical samples with main and different sedimentary facies were selected to conduct experiments of NMR, NMR_C, FE-SEM, LNP, MIP, and SI to analyze the full-spectrum size distribution and connectivity of pores in shale.

2.2. Low-Pressure N_2 Physisorption (LNP). Nitrogen gas adsorption/desorption experiments were carried out with a Micromeritics ASAP 2460 at -196°C (controlled by liquid nitrogen) and relative gas pressure ranging between 0.001 and 0.998. The sample was crushed to 500-841 μm (20-35 mesh), dried in an oven (60°C, 48 hours), and then degassed under high vacuum (<10 mmHg) for 12 hr at 110°C in the apparatus before nitrogen adsorption experiments. The LNP results include the pore surface area calculated from the BET (Brunauer-Emmett-Teller) equation [28], pore volumes determined using the Barrett, Johner, and Halenda (BJH) method [29], and average pore diameter obtained using the ratio between the total amount of adsorbed N_2 and the surface area by assuming cylindrical pore geometry [30].

2.3. NMR and NMR_C Experiments. NMR experiments were conducted on a Niumag MesoMR12-070H-I instrument with a low constant magnetic field of 0.3 T. The experimental parameters were as follows: waiting time (TW) = 5000 ms; echo number (NECH) = 8000; echo interval (TE) = 0.1 ms; and number of scans (NS) = 64. The cylindrical samples (2.54 cm dia. and several centimeters tall) were first dried at 60°C for 48 hr and then saturated with distilled water with the assistance of vacuum pulling for 48 hr at 16 MPa. Both the dry and saturated samples were subjected to NMR T_2 analyses, and the T_2 of dry state served a background value that was subtracted from the saturated T_2, which then yields the actual pore distribution curve.

Based on the relationship between the melting point of the hydrogen and pore size, the NMRc technique can describe the pore size distribution from the linear relation between pore volume and signal intensity [31–33] with the following formula:

$$X = \frac{K_{GT}}{\Delta T}. \quad (1)$$

2.4. MIP Experiments. Utilizing a Micromeritics' AutoPore IV 9520, liquid mercury as a nonwetting fluid for geological porous media was incrementally injected into shale samples with a pressure up to 60,000 psia (413 MPa) to overcome the capillary pressure and occupy the pore space accessible from the sample surface. Assuming that the pores are cylindrical, Washburn [34] determined the pressure to pore-throat relationship from equivalent pressures, and the detectable range of pore-throat sizes is 2.8 nm to 50 μm in diameter for shale samples with porosity of ~5%.

A cube-sized shale sample at 1 cm in length was originally oven dried at 60°C for at least two days to remove any residual moisture in the connected pore space. Then, the samples were placed in a desiccator to cool to room temperature (23°C) with the humidity below 10%. At the beginning of a MIP test, the sample was evacuated until 50 μm Hg pressure (0.05 torr, 0.000972 psi, or 6.7 pa) to remove the air and moisture inside the sample for subsequent mercury intrusion. Then, the sample was subjected to both low- and high-pressure analyses with the equilibration time was set at 10 sec and 60 sec, respectively [35].

2.5. Spontaneous Imbibition. The 1 cm sided cubic samples were oven-dried firstly, and then, four sides of the cubic samples were coated with quick-cure epoxy except for the top and bottom surfaces and dried continuously. After that, the sample's bottom surface was immersed in the fluid with a depth of about 1 mm. The weight of the sample changes with time and was automatically recorded by a high-precision balance, and then, the buoyancy and evaporation were corrected to obtain the liquid mass imbibed into the

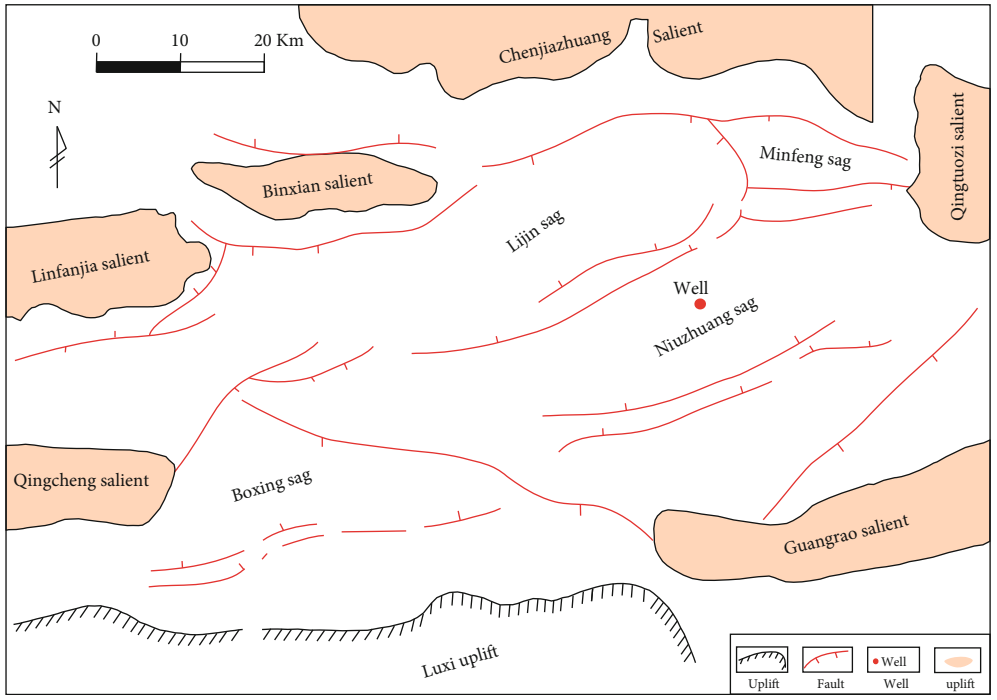

Figure 1: Location map of the study area.

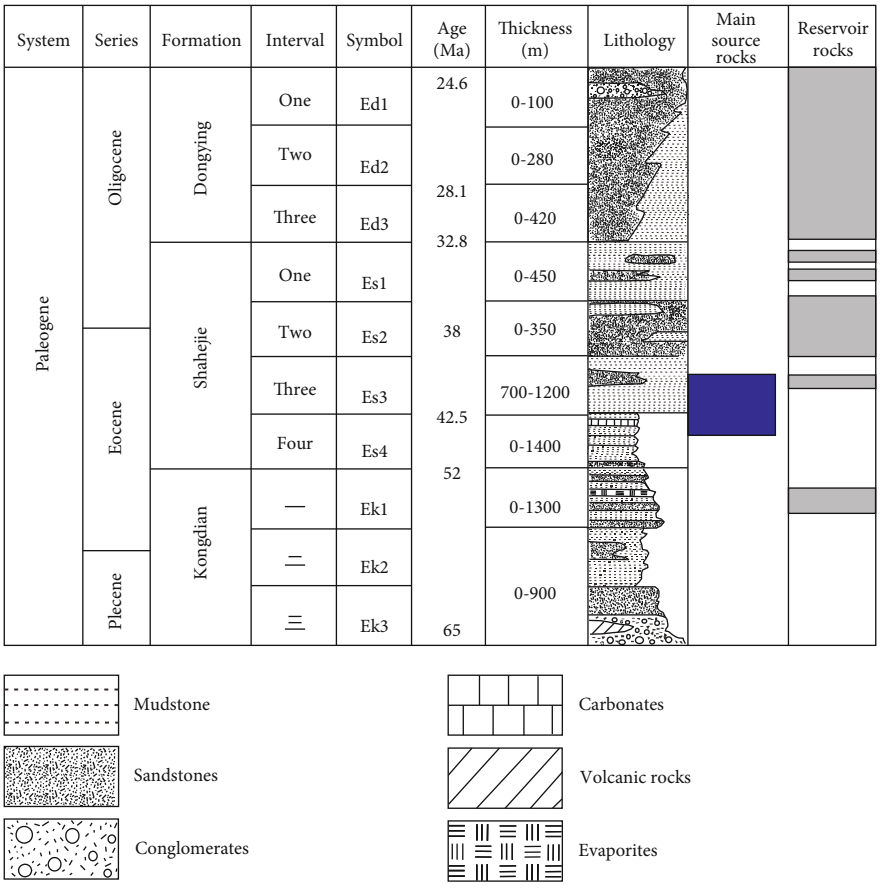

Figure 2: Comprehensive histogram of Cenozoic strata in Dongying sag and sampling depths indicated by the blue rectangle (modified from [27]).

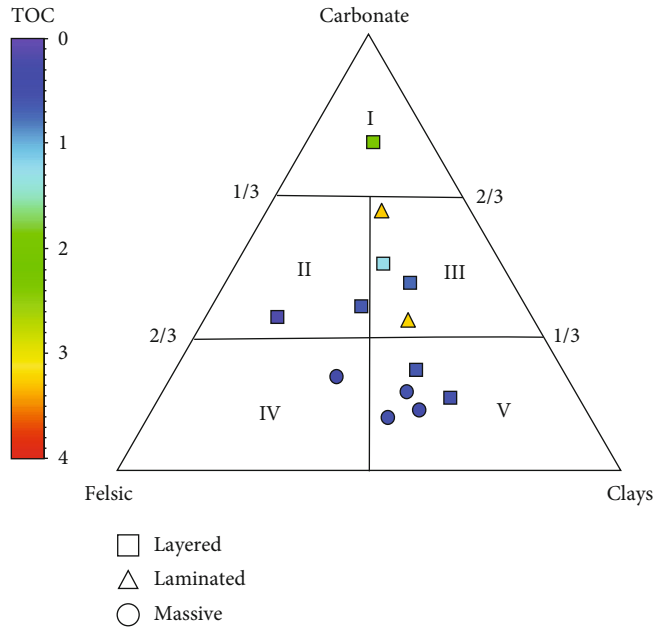

Figure 3: Ternary diagram of mineral compositions and structures of 13 fine-grained Shahejie Shale samples in the upper part of the fourth member, Dongying Sag: I, limestone facies; II, siliceous marlstone facies; III, clayey marlstone facies; IV, siliceous mudstone; V, clayey mudstone facies.

Table 1: Basic properties of shale core samples used for pore structure studies.

Sample ID	Facies	TOC %	Felsic %	Carbonate %	Clays %
X-1	High TOC laminated clayey marlstone	3.2	24.7	34.2	41.1
X-7	Low TOC layered siliceous marlstone	0.18	43.5	30.8	12.2
X-9	Low TOC layered clayey mudstone	0.53	31.6	17.5	46.3
X-11	Low TOC massive siliceous mudstone	0.31	43	20.7	31.1

sample [36]. After about 24 hrs of imbibition, the sample was removed from its contact with the fluid, and weights of sample and fluid reservoir were recorded. Both hydrophilic fluid of deionized water (DIW) and hydrophobic 2DT mixture (decane : toluene = 2 : 1) were used to access their imbibition into water- and oil-wet pore networks.

3. Results and Discussion

3.1. Different Facies of Shale. In terms of mineralogy, organic geochemical parameters (Table 1), and rock sedimentary structure, the following facies classification with different shale oil potentials was established. The minerals in the shale of Dongying Depression are mainly carbonates, felsic, and clay minerals. According to TOC which determines the hydrocarbon generation potential of a mudstone [22], the fine-grained mudstone can be subdivided into the one with high organic matter content (TOC>2%) which can be as high-yield shale reservoirs, medium organic matter content (TOC between 1% and 2%), and low organic matter content (TOC <1%) [9]. In addition, based on the division of massive, layered, and laminated sedimentary structures, the samples were divided into five types of facies (Figure 3): I, the high TOC layered siliceous limestone; II, the low TOC massive siliceous mudstone (sample X-11); III, the high TOC laminated clayey marlstone facies (X-1); IV, the low TOC layered siliceous marlstone facies (X-7); and V, the low TOC layered clayey mudstone (X-9). Among them, the core sample mass of the "high TOC layered siliceous limestone" facies is insufficient, and thus, its reservoir properties could not be analyzed.

3.2. Pore Size Distribution of Shale with Different Facies. Pore size distribution (PSD) is a significant parameter in the evaluation of pore structure, fluid distribution, and enhanced petroleum recovery [37, 38]. The LNP and NMR tests are often used to describe PSD [39, 40].

3.2.1. Characterization of Pore Structure within 100 nm. Figure 4 presents the results of LNP tests for four different facies. The reversed S-shaped adsorption isotherms are similar to type II according to the Brunauer, Deming, and Teller classification [41]. At low relative pressure stage (the relative pressure is close to 0), the isotherms exhibit high adsorption,

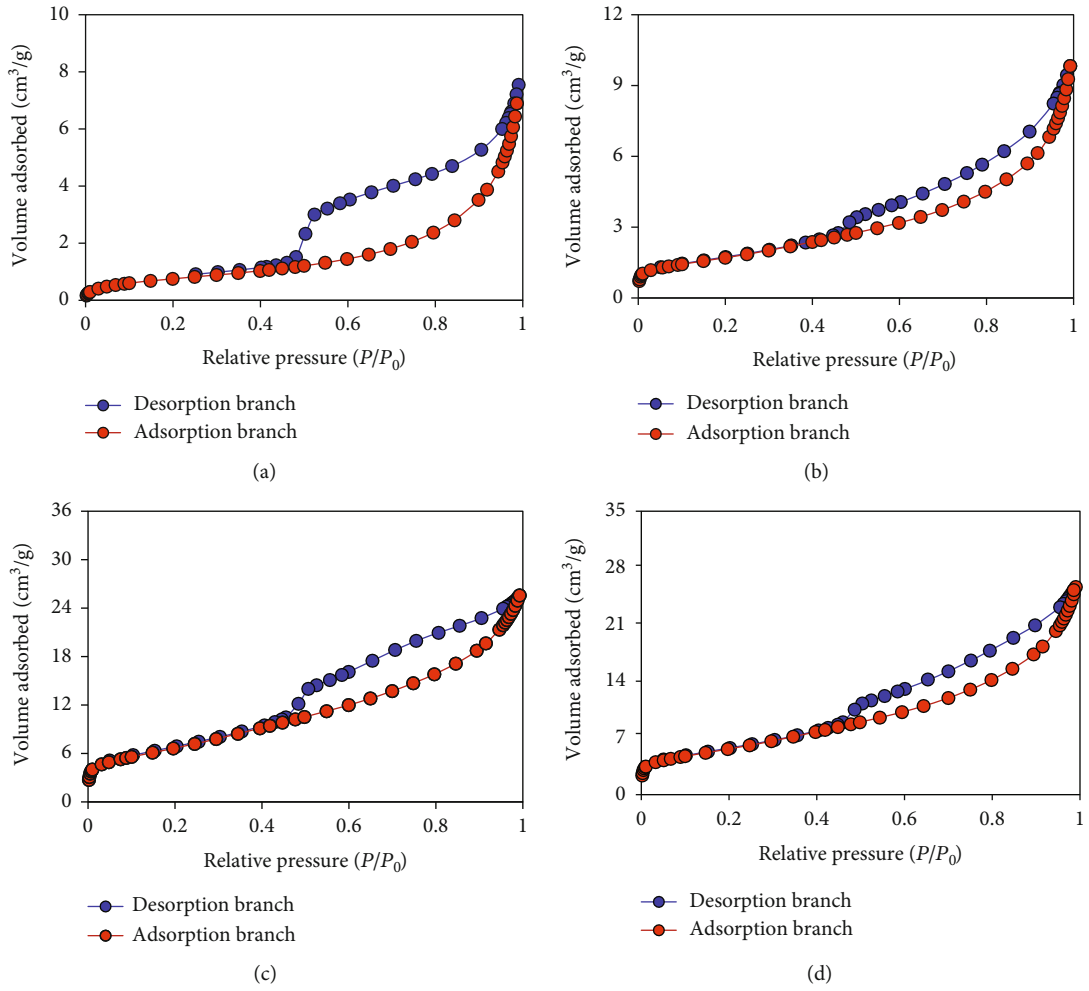

Figure 4: Low-pressure N_2 adsorption-desorption curves.

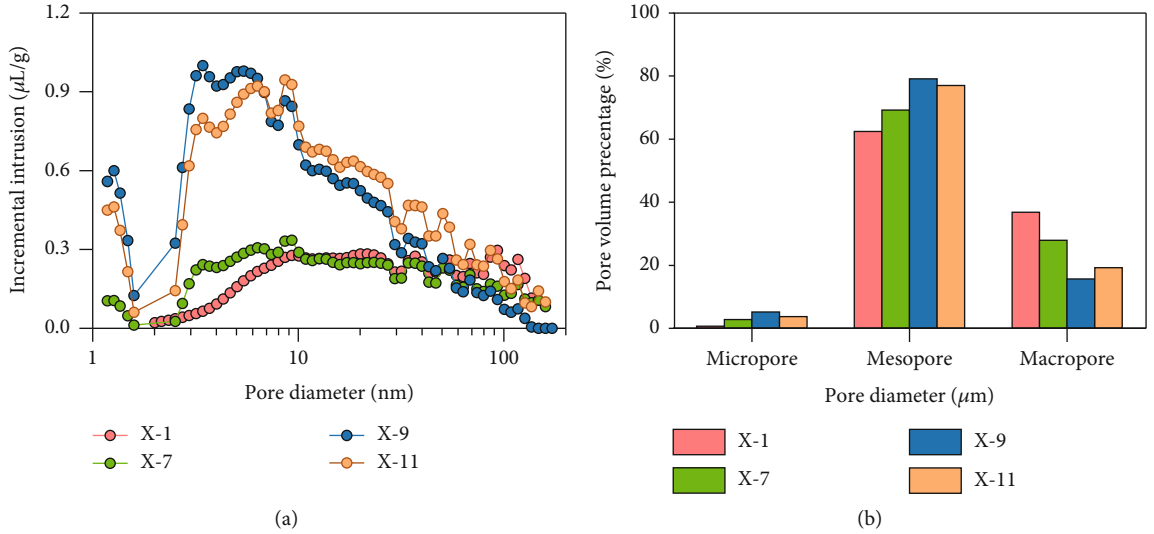

Figure 5: (a) Pore size distribution obtained from N_2 adsorption with DFT. (b) Proportions of micropores (<2 nm), mesopores (2-50 nm), and macropores (>50 nm) in different facies.

Table 2: Main pore structure parameters obtain from LNP tests for four facies.

Sample ID	BET surface area (m^2/g)	Average pore width (nm)	Pore volume (cm^3/100 g)	Micropores (cm^3/100 g)	Mesopores (cm^3/100 g)	Macropores (cm^3/100 g)
X-1	2.86	10.17	1.126	0.00797	0.703	0.4148
X-7	6.29	6.91	1.438	0.0407	0.995	0.402
X-9	24.64	5.43	3.555	0.1852	2.81	0.558
X-11	20.69	6.16	3.657	0.1404	2.799	0.7175

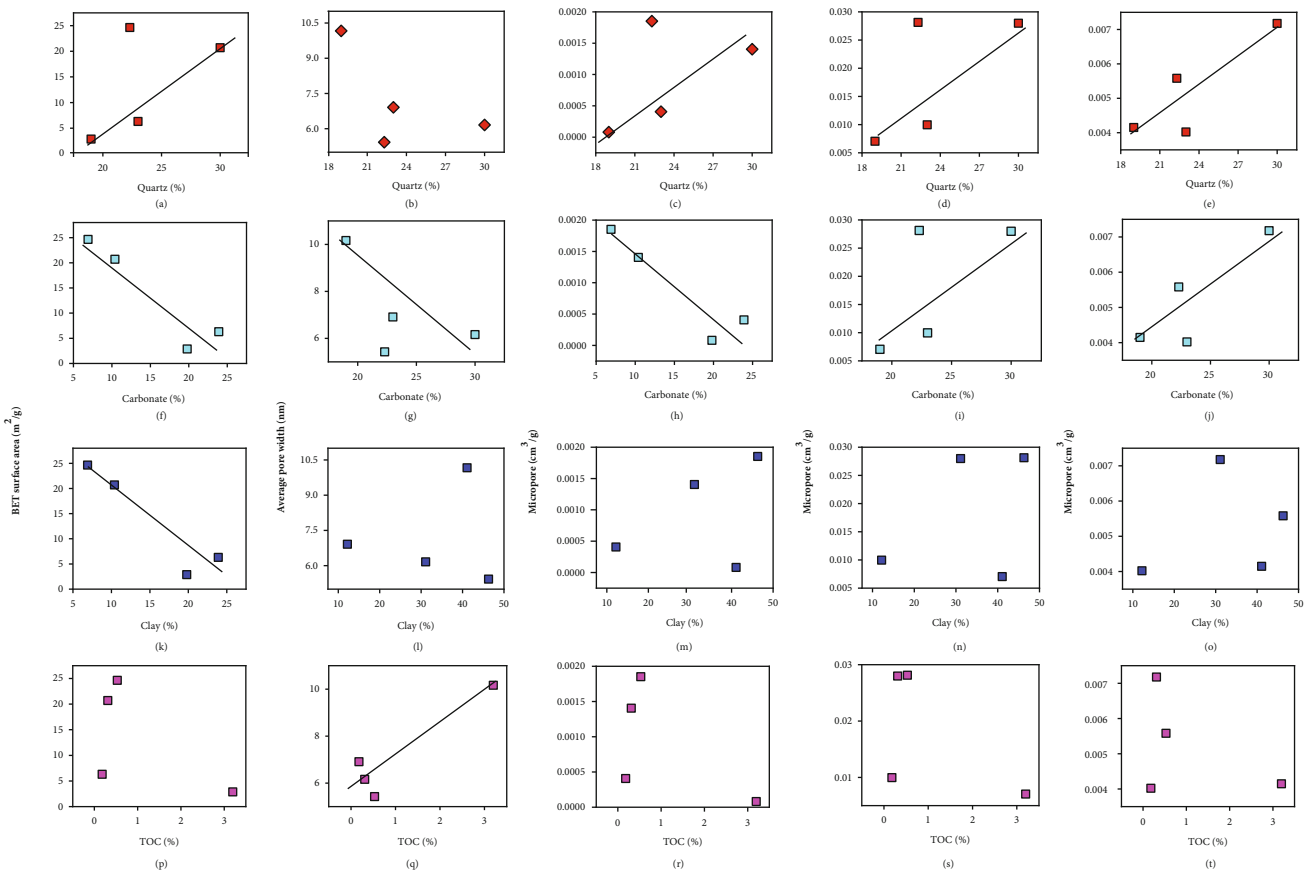

Figure 6: Cross-plots for mineral controls on the development of shale reservoir space.

which may be related to the monolayer adsorption in the micropores. As the relative pressure increases, the N_2 adsorption capacity increases slowly. When the relative pressure increases to 0.9, the N_2 adsorption capacity again increases rapidly, and there is no adsorption saturation, reflecting that there are pores greater than 100 nm in the shales which was characterized by independent NMR tests. The isothermal adsorption and desorption curves of shale begin to separate at a relative pressure of 0.45 and form a hysteresis loop, suggesting the multilayer range associated with capillary condensation in mesopore structures [42, 43]. The curves of the samples are similar to hysteresis loops of H3 and H4, indicating that most of the pores are plate-like pores or ink bottle pores (IUPAC, 1994).

The pore size distributions of four facies calculated from the LNP results with DFT model is given in Figure 5(a). Overall, the "low TOC massive siliceous mudstone" and "low TOC layered clayey mudstone" facies have similar distributions, and the incremental volume is quite higher than the "high TOC laminated clayey marlstone" since the micritic calcite result in the reduction in pore sizes and volumes [44] and the "low TOC layered siliceous marlstone" facies within the 3-30 nm pore size range, which is consistent with the higher N_2 adsorption (Figure 2). According to the IUPAC classifications, pores are divided into micropores (<2 nm), mesopores (2–50 nm), and macropores (>50 nm) (Figure 3(b)), and the proportions of micropores and mesopores of the "low TOC massive siliceous mudstone" and "low TOC layered clayey mudstone" facies are higher than the "high TOC laminated clayey marlstone" and "low TOC layered siliceous marlstone" facies which have a high proportion of macropores (Figure 5(b).

Table 2 present the results of LNP isotherms for four facies. The BET surface areas of the "low TOC layered clayey

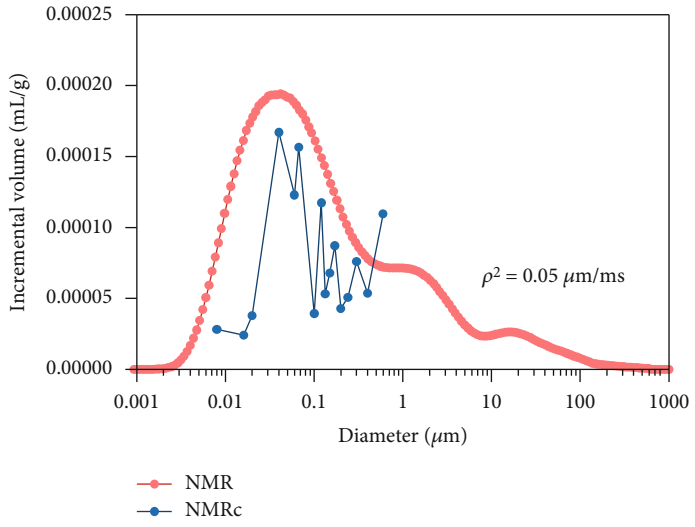

(a)

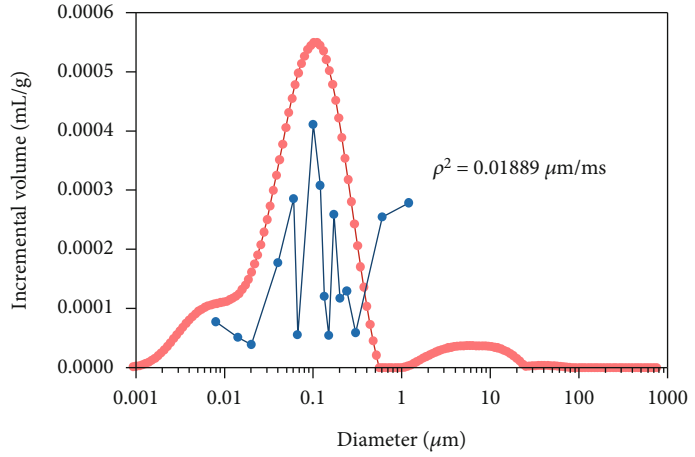

(b)

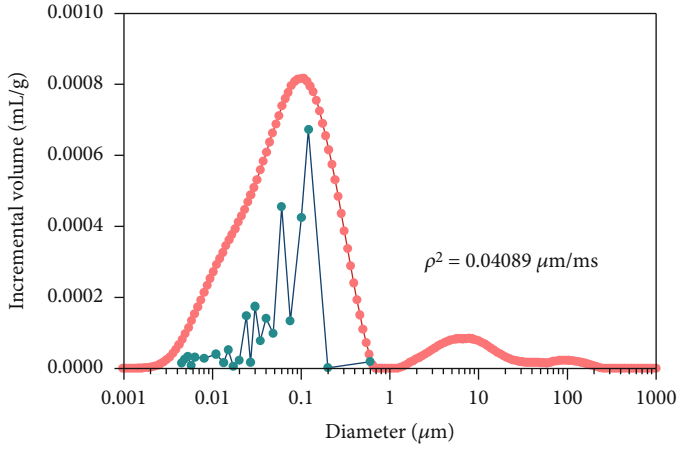

(c)

Figure 7: Continued.

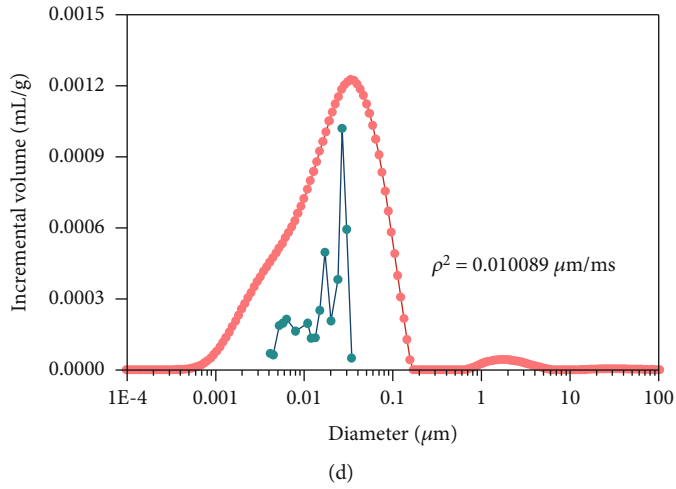

Figure 7: Comparisons of PSD measured by NMR and NMR_C for different samples.

mudstone" and "low TOC massive siliceous mudstone" are 24.6 m^2/g and 20.7 m^2/g, respectively, which are much higher than that of the "high TOC laminated clayey marlstone" and "low TOC layered siliceous marlstone" facies. The pore volumes for the "low TOC layered clayey mudstone" and "low TOC massive siliceous mudstone" facies are 3.56 cm^3/100 g and 3.66 cm^3/100 g, respectively (Table 2), which are also larger than those of the "high TOC laminated clayey marlstone" (1.13 cm^3/100 g) and "low TOC layered siliceous marlstone" X-7 (1.44 cm^3/100 g) facies. However, the average pore width of the "high TOC laminated clayey marlstone" (10.2 nm) and "low TOC layered siliceous marlstone" (6.91 nm) facies are larger than other two facies types, indicating that there are more micropores in the "low TOC layered clayey mudstone" and "low TOC massive siliceous mudstone" facies.

We qualitatively assess the correlation of mineral compositions with pore structure parameters, with an understanding of no-casual link among them and limited sample numbers in this work. Figures 6(a) and 6(c)–6(e) show that quartz is positively correlated with BET surface area, micropores, mesopores, and macropores, and it can be found that there is no correlation between the content of quartz minerals and total pore area. Figures 6(i) and 6(j) show that there is a positive correlation between the content of carbonates and mesopores and macropores, but negative correlation with micropores; in addition, both the BET surface area and average pore width is also negatively correlated with carbonate mineral contents. Figure 6(k) shows that there is a negative correlation between the BET surface area and clay content. Unlike other two minerals, there is no correlation between the content of clay minerals and average pore width and pore volume (Figures 6(l)–6(o)), and the correlation between TOC and pore structure parameters is also generally poor (Figures 6(p)–6(t)).

3.2.2. Full-Spectrum Pore Sizes for Shales with Different Facies. NMR and NMR_C techniques are reliable and effective measurement to characterize pore size distribution [33, 37, 45, 46]. Based on the surface relaxation equation and assumption of cylindrical pore geometry, the NMR method has been used to analyze pore size distribution of shale samples [47, 48]. Equation (2) depicts the relationship between T_2 and different pore sizes [49].

$$r = 2\rho_2 T_2. \tag{2}$$

Parameter ρ_2 (surface relaxivity) is a critical one for converting the T_2 value to pore radius r, which is usually determined by matching the T_2 distribution to the PSD from other laboratory measurements [50]. The measured scale of pore size distribution from the NMR_C (1.7 to 300 nm) is less than NMR T_2 techniques. However, for adsorption pores, the accuracy and resolution of NMR_C is higher than those of NMR [51]. Therefore, in this study, we use NMR_C to obtain the value of surface relaxivity of four facies by correlating the main peaks of NMR and NMR_C (Figure 7).

Different T_2 spectrum peaks of shales indicate a large difference in pore fractures of different facies [44]. Figure 7 illustrates the PSD curves from NMR and NMR_C. The T_2 spectra for the "high TOC laminated clayey marlstone" facies (X-1) commonly show three peaks, with a dominant peak below 300 nm which can be a combination of clay-bound water and water-filling inside the nanosized pores. In addition, there are also a smaller peak in the T_2 spectra around more than 10 μm (Figure 7(a)), which may originate from water inside interlayer cracks and microfractures. The T_2 spectra of other three facies are both characterized by two peaks, and the main peak of the "low TOC layered siliceous marlstone" (sample X-7) and "low TOC layered clayey mudstone" facies has a similar range of 2-500 nm, as compared to 1-30 nm for the "low TOC massive siliceous mudstone" facies.

3.2.3. Pore Morphology of Shales with Different Facies. The classification systems for shale pores are somewhat variable in the literature, Slatt and O'Brien [52] proposed that pores in shale can be divided into organic pores, interparticle flocculation pores, fossil clastic pores, fecal pellet pores, mineral grain intraparticle pores, and microfractures. In

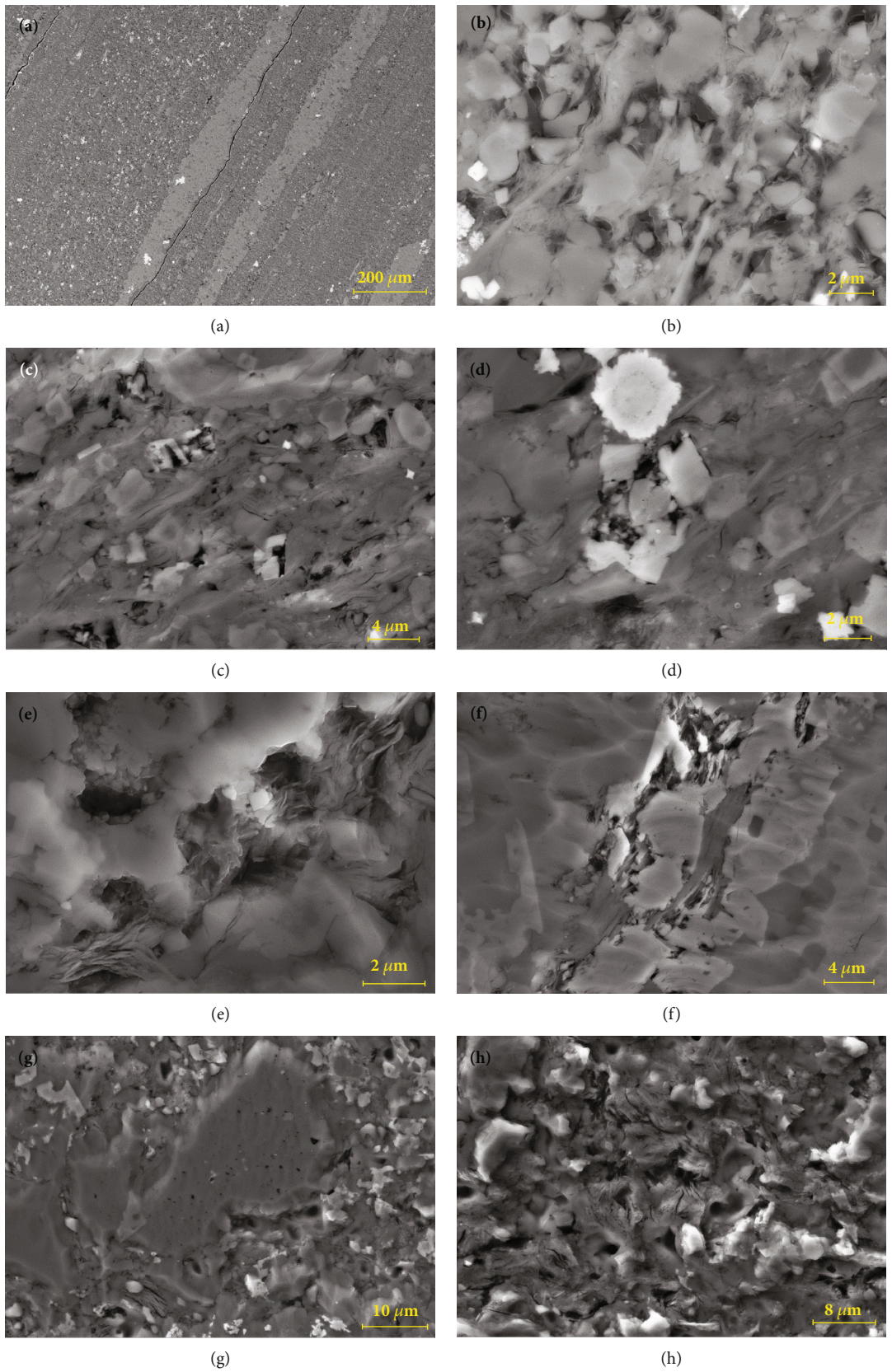

Figure 8: FE-SEM images of samples from the Dongying Depression: (a) calcite laminae and fractures; (b) organic pores; (c) intergranular pores; (d) intercrystalline pores of clay minerals; (e) dolomite dissolution pore; (f) dissolution and organic pores; (g) intragranular pores; and (h) intergranular pores.

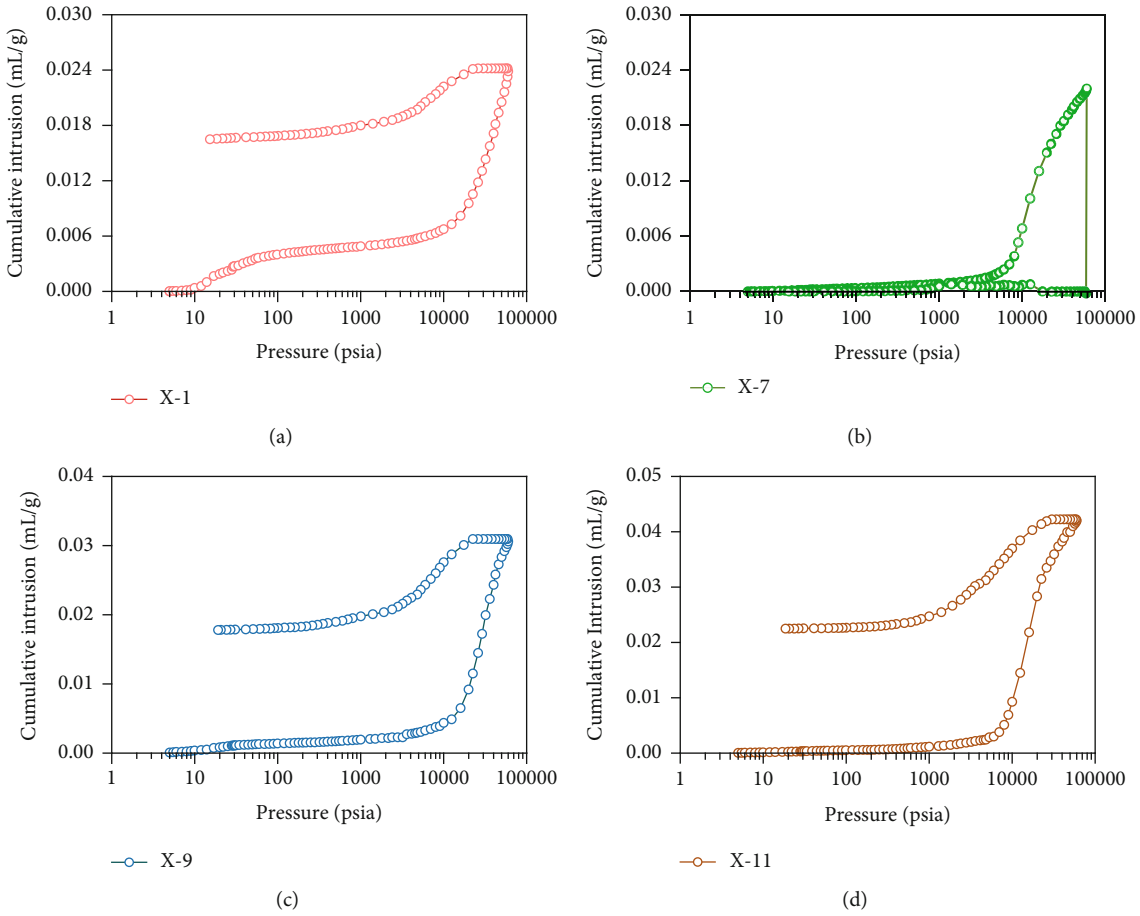

Figure 9: Hysteresis curves of drainage (mercury intrusion) and imbibition (mercury extrusion) from MIP tests.

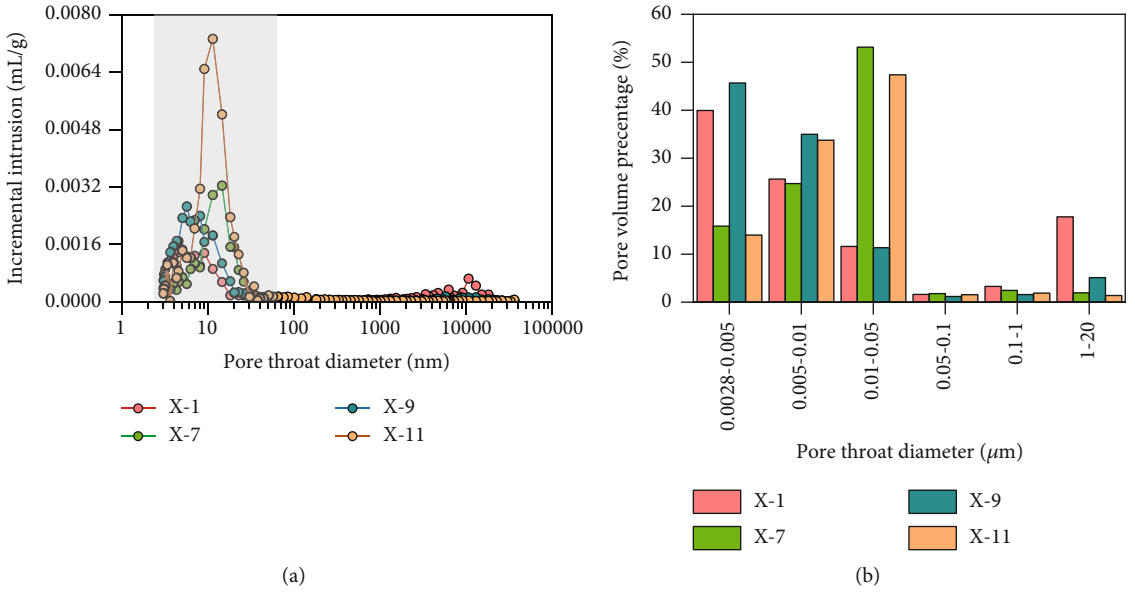

Figure 10: Pore-throat distribution curves as derived from MIP tests (a) and proportions of pore-throat sizes (b) in four samples with different facies.

Table 3: Main pore structure parameters obtain from MIP tests for four facies.

Sample ID	Total pore volume (cm^3/g)	Total pore area (m^2/g)	Median pore diameter by volume (nm)	Average pore-throat diameter (nm)	Porosity (%)
X-1	0.0239	13.58	6.89	7.03	5.69
X-7	0.022	8.813	13.54	9.97	5.73
X-9	0.0297	19.629	5.97	6.05	7.36
X-11	0.042	14.538	14.61	11.55	9.66

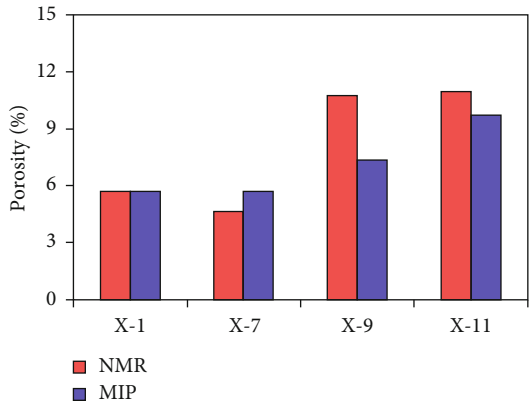

Figure 11: Porosity results from MIP and NMR tests for four facies.

addition, Loucks [53] divided the shale reservoir spaces into three types: intraparticle, interparticle, and organic-matter pores.

The "high TOC laminated clayey marlstone" facies contains abundant calcite laminae which have a good connectivity (Figure 8(a)), and organic matter-hosted pores are at several to hundreds of nanometers in diameters (Figure 8(b)), which is consistent with the findings of Zhang [44]. The "low TOC layered siliceous marlstone" facies (sample X-7) is characterized by both intergranular and intercrystalline pores (Figures 8(c) and 8(d)), and the intergranular pores developed between mineral particles [54] are usually well connected to form an effective pore network which is beneficial to the migration of oil and gas [53]. The intercrystalline pores along clay layers are well developed (Figure 8(d)). However, clay minerals have dual effects on pore development, which will negatively affect the generation of intergranular pores [55], but can generate intercrystalline pores (Figure 8(d)), making the relationship between clay mineral content and pore space complex [56]. The "low TOC layered clayey mudstone" facies dominantly contains interparticle pores and dolomite dissolution pores and is also composed of organic matter-hosted pores (Figures 8(e) and 8(f)). The nonstable (e.g., carbonates) minerals are dissolved by acidic fluid created when organic matter generates hydrocarbon [57]. The "low TOC massive siliceous mudstone" facies mainly develops intragranular pores and intergranular pores, in which the pore connectivity in quartz particles is poor (Figures 8(g) and 8(h)).

3.3. Pore Connectivity Characteristics of Shale

3.3.1. Characterization of Pore Connectivity for Shale by Nonwetting Phase Mercury. The cumulative intrusion-extrusion curves from the MIP technique are presented in Figure 9, which shows that approximately 60% of the intruded mercury remains trapped inside the pore spaces after extrusion as an obvious loop for different shale samples. The "low TOC massive siliceous mudstone" facies has the highest mercury intrusion volume at the maximum pressure suggesting a much higher amount of fine mesopore volumes (a pore-throat diameter range of 3–10 nm), followed by the "low TOC layered clayey mudstone" facies.

The pore-throat size distributions obtained from the MIP tests play an important role for petroleum movement, and the linkage of smaller nanopores is shown in Figure 10. Pores in these four samples of different facies are mainly on the nanoscale and predominated by pore-throat diameters less than 50 nm. But in the range of >1 μm, the "high TOC laminated clayey marlstone" facies exhibits a noticeable peak (Figure 10(a)) and associated volume proportion (Figure 10(b)), possibly because the interlaminar structure and microcracks largely contribute to the 1–20 μm pores; thus, this facies could have a good connectivity for μm-scaled pore networks.

Table 3 shows that the total pore volume of four types of facies ranges at 0.022 to 0.042 cm^3/g, the total pore area is 8.81-19.6 m^2/g, and the median diameter and average pore-throat diameter are 6.05-11.6 nm and 5.69-9.66 nm, respectively. The porosities obtained from mercury injection (Table 3) are from 5.69% to 9.66%, and the "low TOC layered clayey mudstone" and "low TOC massive siliceous mudstone" facies have higher porosity than other facies, and this is consistent with the results from NMR tests (Figure 11).

Figures 12(a), 12(c), 12(d), and 12 (e) show that quartz is positively correlated with total pore volume, median pore diameter, and average pore diameter, and there is no correlation between the content of quartz minerals and the total pore area (Figure 12(b)). The total pore volume and total pore area are negatively correlated with carbonate mineral content (Figures 12(e) and 12(f)). Figure 12(j) shows that there is a good linear and positive correlation between the total pore area and clay content. On the contrary, with the increase of clay contents, the median pore diameter and average pore diameter decrease. Unlike the other two mineral composition, clays have no obvious correlation with total pore volume (Figure 12(i)).

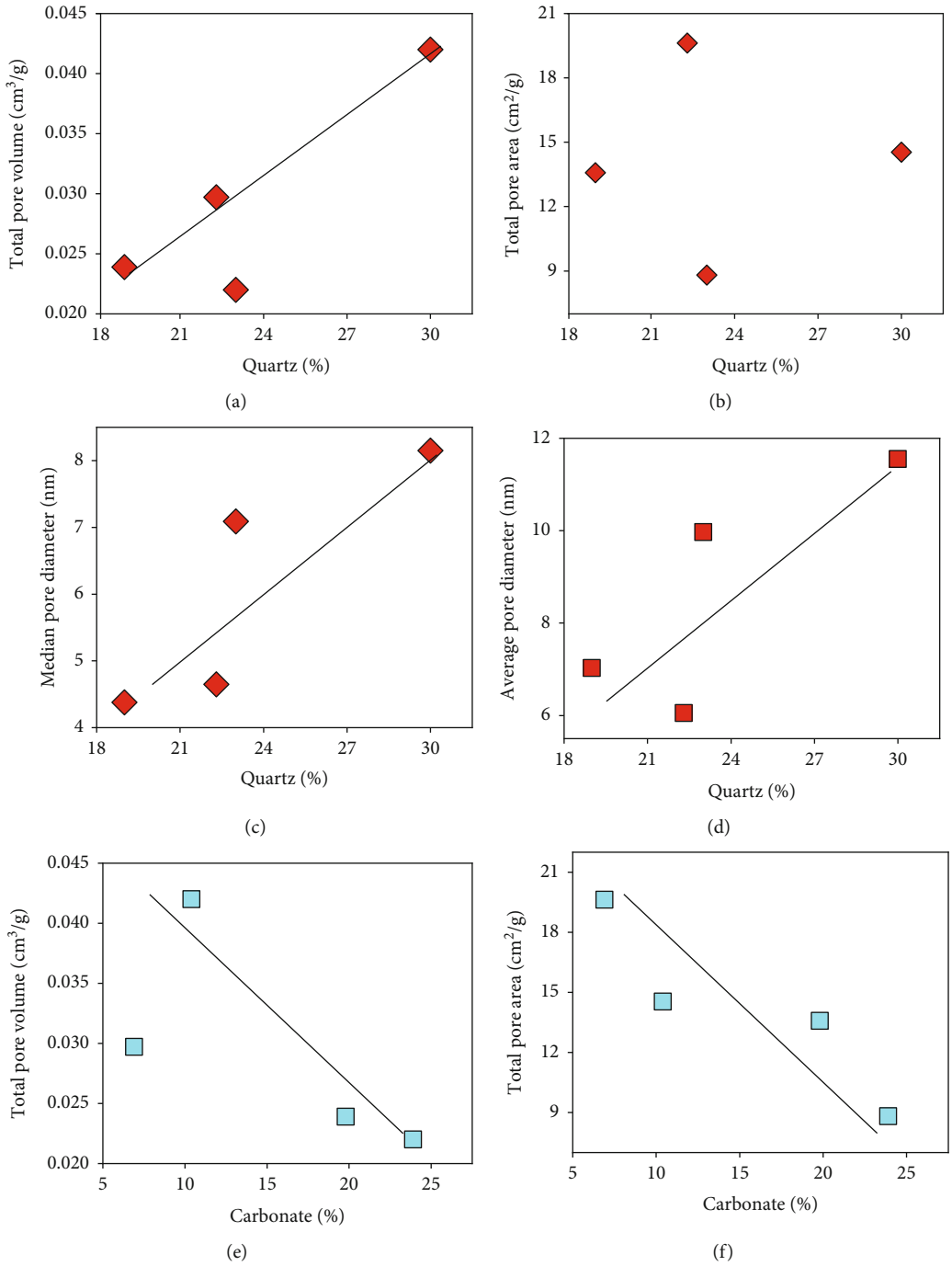

Figure 12: Continued.

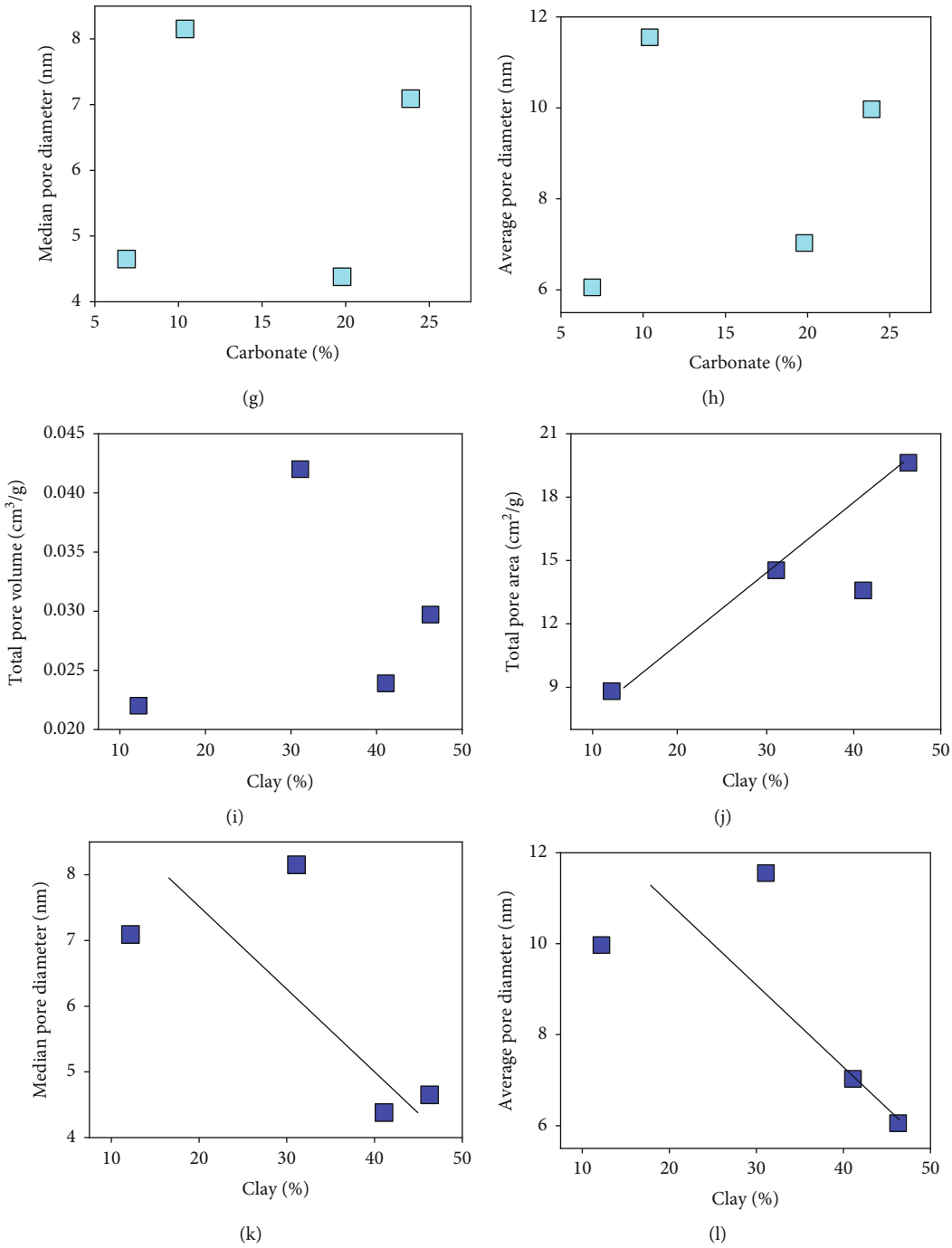

Figure 12: Relationship between MIP-derived total pore volume (a, e, and i), total pore area (b, f, and j), mediam pore diameter (c, g, and k), and average pore diameter (d, h, and l)" for better clarification.

3.3.2. Characterization of Pore Connectivity for Shale by Wetting Phase Fluid. The spontaneous imbibition process is an effective and simple procedure to analyze the connectivity of porous media towards a testing fluid [13, 58, 59]. The main driving force of the imbibition process is the gradient of capillary force [34, 60]. Figure 13 compares the log-log plots of cumulative imbibition for DIW and 2DT. The imbibition curves of DIW are divided into two stages (stages I and II) [61].

The stage I is usually a linear segment with different imbibition slopes for distinct facies [62]. After that, a larger slope value indicating a higher imbibition rate is observed in stage II, probably suggesting that the imbibed fluid gradually migrates from the connected pore space with larger pore sizes to smaller ones in the shale matrix [62]. In contrast to DIW imbibition, 2DT imbibition from duplicate experiments exhibits much lower slopes in stage II for these four as-received (e.g., nonoil washed) samples.

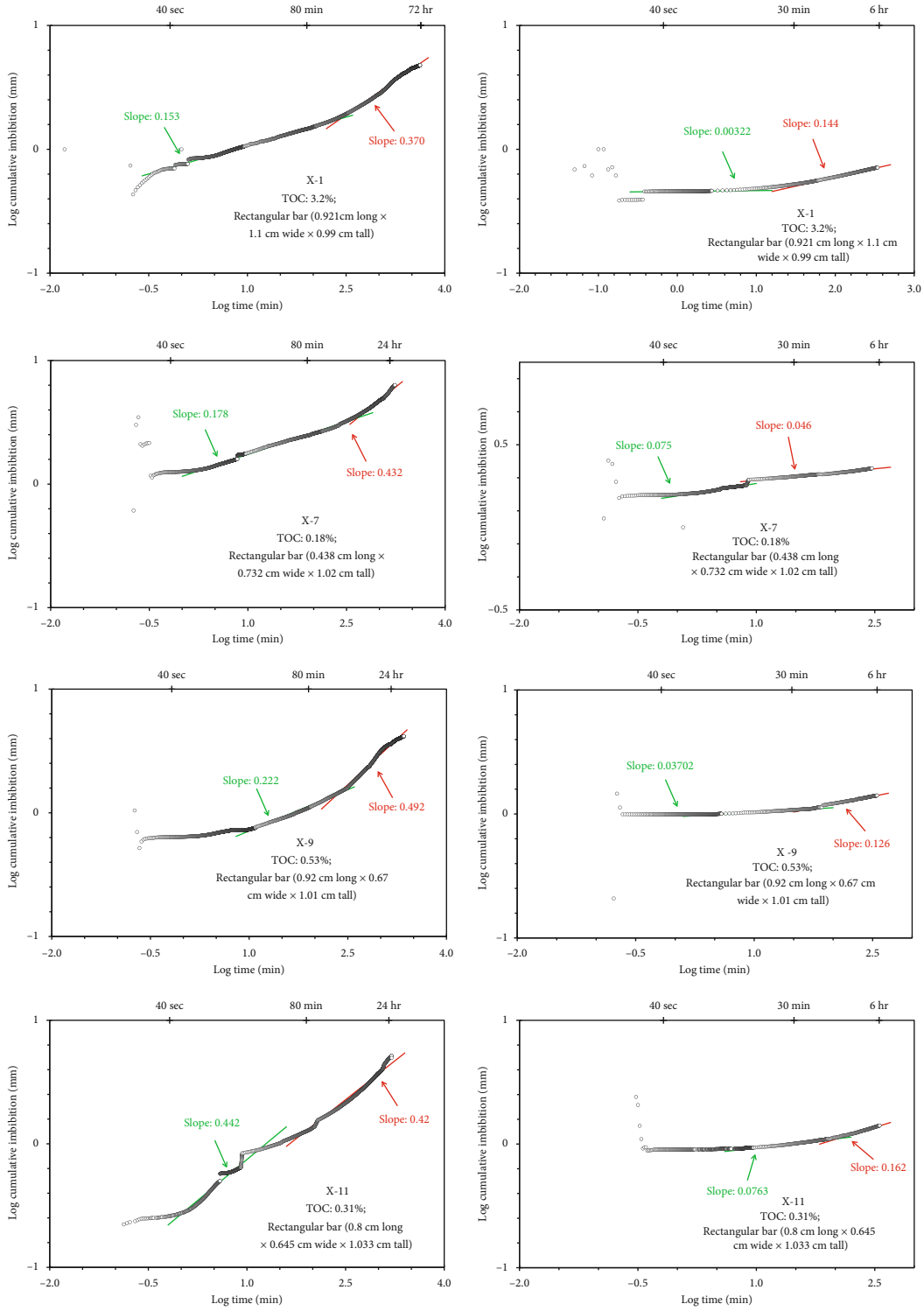

Figure 13: Log-log plots of cumulative elapsed time vs. fluid imbibition (DIW: left panel; 2DT: right panel).

The second imbibition slopes (shown as red colors) in the log-log plots are used to quantitatively assess mudstone's pore connectivity according to the percolation theory [13], and a classical behavior of 0.5 slope value represents high pore connectivity and a slope of 0.26–0.5 for intermediate pore connectivity; the slope below 0.26 means low pore connectivity. Figure 12 shows that the second slopes for DIW imbibition in the "low TOC layered clayey mudstone" and "low TOC massive siliceous mudstone" facies are 0.49 and 0.42, respectively, suggesting that the hydrophilic pore networks have a good connectivity in mm-scale sample sizes. The hydrophilic pores of the "high TOC laminated clayey

marlstone" and "low TOC layered siliceous marlstone" facies have an intermediate connectivity. However, the 2DT imbibition for all of four facies show low slopes of <0.26. In addition, the "low TOC layered siliceous marlstone" facies (sample X-7) exhibits even lower imbibition slopes, indicating that the hydrophobic pore networks are poor-connected probably resulting from the absence of the organic matter which is often deemed as a hydrophobic component [63]. Overall, the results indicate that these shale samples from the upper fourth member of Shahejie Formation have well-connected hydrophilic pore networks and poorly connected hydrophobic pores, which are closely related to the mineral composition and the choice of fluids, though many other studies on other shale commonly indicate a better wettability for oil- than water-wet fluids [64–67].

4. Conclusions

A total of 13 shale samples from the upper fourth member of Shahejie Formation in Dongying Depression, Bohai Bay Basin, East China, were collected to study the full-spectrum pore size by combined tests of LNP, NMR, NMR_C, and connectivity properties by the MIP and SI. The "high TOC laminated clayey marlstone" facies has the lowest pore volume and BET surface area within the 3-30 nm pore size range, and NMR T_2 spectrum shows three peaks, with a dominant peak below 300 nm and good connectivity. Pores mainly range at 2 nm to 500 nm with predominant pore-throat diameters of less than 50 nm for the "low TOC layered siliceous marlstone" facies with a low hydrophilic pore connectivity and exhibit weak hydrophobic pore networks, and they both have an intermediate hydrophilic pores connectivity and lower hydrophobic pore networks; the main peak of the "low TOC layered clayey mudstone" facies is located at 2 nm to 500 nm and but for the "low TOC massive siliceous mudstone" is lower at 1-30 nm.

More research is needed in order to increase the validity of the interpretations from this work; for samples with high organic matter contents and in mature windows, oil washing is needed to obtain more accurate information of full-spectrum pore size distribution and connectivity among differently sized pores [21, 68].

Data Availability

The laboratory data used to support the findings of this study are included within the article.

Conflicts of Interest

The authors declare that they have no conflicts of interest.

Acknowledgments

This work was funded by the National Natural Science Foundation of China (Grant No. 41830431) and Shandong Provincial Major Type Grant for Research and Development from the Department of Science & Technology of Shandong Province (Grant No. 2020ZLYS08).

References

[1] K. A. Bowker, "Barnett shale gas production, Fort Worth basin: issues and discussion," *AAPG Bulletin*, vol. 91, no. 4, pp. 523–533, 2007.

[2] B. J. Cardott, "Thermal maturity of Woodford shale gas and oil plays, Oklahoma, USA," *International Journal of Coal Geology*, vol. 103, no. 103, pp. 109–119, 2012.

[3] Q. H. Hu, R. P. Ewing, and H. D. Rowe, "Low nanopore connectivity limits gas production in Barnett formation," *Journal of Geophysical Research - Solid Earth*, vol. 120, no. 12, pp. 8073–8087, 2015.

[4] S. Y. Hu, B. Bai, S. Z. Tao et al., "Heterogeneous geological conditions and differential enrichment of medium and high maturity continental shale oil in China," *Petroleum Exploration and Development*, vol. 49, no. 2, pp. 257–271, 2022.

[5] D. M. Jarvie, R. J. Hill, T. E. Ruble, and R. M. Pollastro, "Unconventional shale-gas systems: the Mississippian Barnett shale of north-Central Texas as one model for thermogenic shale-gas assessment," *AAPG Bulletin*, vol. 91, no. 4, pp. 475–499, 2007.

[6] Z. Jiang, W. Zhang, C. Liang, Y. Wang, H. Liu, and X. Chen, "Characteristics and evaluation elements of shale oil reservoir," *Acta Petrolei Sinica*, vol. 35, no. 1, pp. 184–196, 2014.

[7] X. Wu, B. Gao, X. Ye, R. Bian, H. Nie, and F. Lu, "Shale oil accumulation conditions and exploration potential of faulted basins in the east of China," *Oil and Gas Geology*, vol. 34, no. 4, pp. 455–462, 2013.

[8] Q. Zhou and G. Yang, "Definition and application of tight oil and shale oil terms," *Oil and Gas Geology*, vol. 33, no. 4, pp. 541–544, 2012.

[9] C. Zou, Z. Yang, J. Cui et al., "Formation mechanism, geological characteristics, and development strategy of nonmarine shale oil in China," *Petroleum Exploration and Development*, vol. 40, no. 1, pp. 15–27, 2013.

[10] L. Sun, X. Wang, X. Jin, J. M. Li, and S. T. Wu, "Three dimensional characterization and quantitative connectivity analysis of micro/nano pore space," *Petroleum Exploration and Development*, vol. 44, no. 2, pp. 490–498, 2016.

[11] R. Y. Sun, G. Y. Tang, D. J. Gong, S. F. Yao, and D. F. Du, "Multi-mechanism coupling seepage in shale gas reservoir," *Science, Technology and Engineering*, vol. 16, no. 34, pp. 64–69, 2016.

[12] L. Bai, B. Liu, J. Yang, S. Tian, B. Wang, and S. Wang, "Differences in hydrocarbon composition of shale oils in different phase states from the Qingshankou formation, Songliao basin, as determined from fluorescence experiments," *Frontiers in Earth Science*, vol. 15, no. 2, pp. 438–456, 2021.

[13] Q. H. Hu, R. P. Ewing, and S. Dultz, "Low pore connectivity in natural rock," *Journal of Contaminant Hydrology*, vol. 133, no. 5, pp. 76–83, 2012.

[14] H. K. Nie, J. C. Zhang, and Y. Li, "Accmulation conditions of the lower Cambrian shale gas in the Sichuan Basin and its periphery," *Acta Petrolei Sinica*, vol. 32, no. 6, pp. 959–967, 2011.

[15] C. Zou, R. Zhu, S. Wu et al., "Types, characteristics, genesis and prospects of conventional and unconventional hydrocarbon accumulations: taking tight oil and tight gas in China as an instance," *Acta Petrolei Sinica*, vol. 33, no. 2, pp. 173–187, 2012.

[16] B. Thyberg, J. Jahren, T. Winje, K. Bjørlykke, J. I. Faleide, and Ø. Marcussen, "Quartz cementation in Late Cretaceous

mudstones, northern North Sea: changes in rock properties due to dissolution of smectite and precipitation of microquartz crystals," *Marine and Petroleum Geology*, vol. 27, no. 8, pp. 1752–1764, 2010.

[17] G. R. Chalmers, R. M. Bustin, and I. M. Power, "Characterization of gas shale pore systems by porosimetry, pycnometry, surface area, and field emission scanning electron microscopy/transmission electron microscopy image analyses: examples from the Barnett, Woodford, Haynesville, Marcellus, and Doig units," *AAPG Bulletin*, vol. 96, no. 6, pp. 1099–1119, 2012.

[18] R. Yang, S. He, J. Yi, and Q. Hu, "Nano-scale pore structure and fractal dimension of organic-rich Wufeng-Longmaxi shale from Jiaoshiba area, Sichuan basin: investigations using FE-SEM, gas adsorption and helium pycnometry," *Marine and Petroleum Geology*, vol. 70, pp. 27–45, 2016.

[19] J. Lai, G. Wang, Z. Wang et al., "A review on pore structure characterization in tight sandstones," *Earth-Science Reviews*, vol. 177, pp. 436–457, 2018.

[20] R. Yang, F. Hao, S. He et al., "Experimental investigations on the geometry and connectivity of pore space in organic-rich Wufeng and Longmaxi shales," *Marine and Petroleum Geology*, vol. 84, pp. 225–242, 2017.

[21] L. Bai, B. Liu, Y. Du et al., *Distribution Characteristics and Oil Mobility Thresholds in Lacustrine Shale Reservoir: Insights from N_2 Adsorption Experiments on Samples Prior to and Following Hydrocarbon Extraction*, Petrol, 2021.

[22] W. W. Li, J. Cao, C. H. Shi, T. W. Xu, H. G. Zhang, and Y. X. Zhang, "Shale oil in saline lacustrine systems: a perspective of complex lithologies of fine-grained rocks," *Marine and Petroleum Geology*, vol. 116, article 104351, 2020.

[23] B. Liu, J. Sun, and Y. Zhang, "Reservoir space and enrichment model of shale oil in the first member of Cretaceous Qingshankou formation in the Changling sag, southern Songliao Basin, NE China," *Petroleum Exploration and Development*, vol. 48, no. 3, pp. 608–624, 2021.

[24] X. W. Zheng, B. Q. Zhang, H. Saneia et al., "Pore structure characteristics and its effect on shale gas adsorption and desorption behavior," *Marine and Petroleum Geology*, vol. 100, pp. 165–178, 2019.

[25] G. Chen, S. Lu, J. Zhang et al., "Estimation of enriched shale oil resource potential in E2s4L of Damintun sag in Bohai Bay basin, China," *Energy & Fuels*, vol. 31, no. 4, pp. 3635–3642, 2017.

[26] Z. Z. Feng, "A review on the definitions of terms of sedimentary facies," *Journal of Palaeogeography*, vol. 8, no. 1, p. 32, 2019.

[27] X. W. Guo, K. Y. Liu, S. He et al., "Petroleum generation and charge history of the northern Dongying depression, Bohai Bay basin, China: insight from integrated fluid inclusion analysis and basin modelling," *Marine and Petroleum Geology*, vol. 32, no. 1, pp. 21–35, 2012.

[28] S. Brunauer, P. H. Emmett, and E. J. Teller, "Adsorption of gases in multimolecular layers," *Journal of the American Chemical Society*, vol. 60, no. 2, pp. 309–319, 1938.

[29] E. P. Barrett, L. G. Joyner, and P. P. Halenda, "The determination of pore volume and area distributions in porous substances. I. Computations from nitrogen isotherms," *Journal of the American Chemical Society*, vol. 73, no. 1, pp. 373–380, 1951.

[30] M. M. Labani, R. Rezaee, A. Saeedi, and H. A. Al, "Evaluation of pore size spectrum of gas shale reservoirs using low pressure nitrogen adsorption, gas expansion and mercury porosimetry: a case study from the Perth and Canning basins, Western Australia," *Journal of Petroleum Science and Engineering*, vol. 112, pp. 7–16, 2013.

[31] J. Mitchell, J. B. W. Webber, and J. H. Strange, "Nuclear magnetic resonance cryoporometry," *Physics Reports*, vol. 461, no. 1, pp. 1–36, 2008.

[32] J. B. W. Webber, P. Corbett, K. T. Semple et al., "An NMR study of porous rock and biochar containing organic material," *Microporous and Mesoporous Materials*, vol. 178, pp. 94–98, 2013.

[33] Y. Zhao, Y. Sun, S. Liu, K. Wang, and Y. Jiang, "Pore structure characterization of coal by NMR cryoporometry," *Fuel*, vol. 190, pp. 359–369, 2017.

[34] E. W. Washburn, "The dynamics of capillary flow," *Physics Review*, vol. 17, no. 3, pp. 273–283, 1921.

[35] Q. H. Hu, Y. X. Zhang, X. H. Meng, Z. Li, Z. H. Xie, and M. W. Li, "Characterization of micro-nano pore networks in shale oil reservoirs of Paleogene Shahejie formation in Dongying sag of Bohai Bay basin, East China," *Petroleum Exploration and Development*, vol. 44, no. 5, pp. 720–730, 2017.

[36] Q. H. Hu, P. Persoff, and J. S. Y. Wang, "Laboratory measurement of water imbibition into low-permeability welded tuff," *Journal of Hydrology*, vol. 242, no. 1–2, pp. 64–78, 2001.

[37] X. Li, Y. Kang, and M. Haghighi, "Investigation of pore size distributions of coals with different structures by nuclear magnetic resonance (NMR) and mercury intrusion porosimetry (MIP)," *Measurement*, vol. 116, pp. 122–128, 2018.

[38] Y. Meng and Z. Li, "Experimental study on diffusion property of methane gas in coal and its influencing factors," *Fuel*, vol. 185, pp. 219–228, 2016.

[39] Y. Cai, Q. Li, D. Liu, Y. Zhou, and D. Lv, "Insights into matrix compressibility of coals by mercury intrusion porosimetry and N_2 adsorption," *International Journal of Coal Geology*, vol. 200, pp. 199–212, 2018.

[40] C. Peng, C. Zou, Y. Yang, G. Zhang, and W. Wang, "Fractal analysis of high rank coal from southeast qinshui basin by using gas adsorption and mercury porosimetry," *Journal of Petroleum Science and Engineering*, vol. 156, pp. 235–249, 2017.

[41] S. Brunauer, L. S. Deming, W. E. Deming, and E. Teller, "On a theory of the van der Waals adsorption of gases," *Journal of the American Chemical Society*, vol. 62, no. 7, pp. 1723–1732, 1940.

[42] J. Rouquerol, D. Avnir, C. Fairbridge et al., "Recommendations for the characterization of porous solids (technical report)," *Pure and Applied Chemistry*, vol. 66, no. 8, pp. 1739–1758, 1994.

[43] M. Thommes, K. Kaneko, A. V. Neimark et al., "Physisorption of gases, with special reference to the evaluation of surface area and pore size distribution (IUPAC technical report)," *Pure and Applied Chemistry*, vol. 87, no. 9-10, pp. 1051–1069, 2015.

[44] S. Zhang, H. M. Liu, M. Wang et al., "Shale pore characteristics of Shahejie formation: implication for pore evolution of shale oil reservoirs in Dongying sag, North China," *Petroleum Research*, vol. 4, no. 2, pp. 113–124, 2019.

[45] Y. Yao and D. Liu, "Comparison of low-field NMR and mercury intrusion porosimetry in characterizing pore size distributions of coals," *Fuel*, vol. 95, no. 1, pp. 152–158, 2012.

[46] M. Zou, C. Wei, Z. Miao, S. Jian, Y. Chen, and Q. Yu, "Classifying coal pores and estimating reservoir parameters by

nuclear magnetic resonance and mercury intrusion porosimetry," *Energy & Fuels*, vol. 27, no. 7, pp. 3699–3708, 2013.

[47] X. Jin, X. Wang, X. Liu et al., "Low field cryoporometry NMR for mesopores distribution in shale," in *SPE/IATMI Asia Pacific Oil & Gas Conference and Exhibition*, Jakarta, Indonesia, 2017.

[48] A. Li, W. Ding, R. Wang et al., "Petrophysical characterization of shale reservoir based on nuclear magnetic resonance (NMR) experiment: a case study of lower Cambrian Qiongzhusi formation in eastern Yunnan province, South China," *Journal of Natural Gas Science and Engineering*, vol. 37, pp. 29–38, 2017.

[49] C. H. Sondergeld, R. J. Ambrose, C. S. Rai, and J. Moncrieff, "Micro-structural studies of gas shales," in *SPE unconventional gas conference*, Pittsburgh, Pennsylvania, USA, 2010.

[50] R. L. Kleinberg, "Utility of NMR T2 distributions, connection with capillary pressure, clay effect, and determination of the surface relaxivity parameter $\rho 2$," *Magnetic Resonance Imaging*, vol. 14, no. 7-8, pp. 761–767, 1996.

[51] T. Yin, D. Liu, and Y. Cai, "Size distribution and fractal characteristics of coal pores through nuclear magnetic resonance cryoporometry," *Energy & Fuels*, vol. 31, no. 8, pp. 7746–7757, 2017.

[52] R. M. Slatt and N. R. O'Brien, "Pore types in the Barnett and Woodford gas shales: contribution to understanding gas storage and migration pathways in fine-grained rocks," *AAPG Bulletin*, vol. 95, no. 12, pp. 2017–2030, 2011.

[53] R. G. Loucks, R. M. Reed, S. C. Ruppel, and U. Hammes, "Spectrum of pore types and networks in mudrocks and a descriptive classification for matrix-related mudrock pores," *AAPG Bulletin*, vol. 96, no. 6, pp. 1071–1098, 2012.

[54] H. Zhu, Y. Ju, Y. Qi, C. Huang, and L. Zhang, "Impact of tectonism on pore type and pore structure evolution in organic-rich shale: implications for gas storage and migration pathways in naturally deformed rocks," *Fuel*, vol. 228, pp. 272–289, 2018.

[55] H. Huang, J. Chen, Y. Deng, and X. Wang, "Types and influencing factors of pores in Chang 7 continental shale matrix of South Ordos Basin. J. Xi'an Shiyou Univ," *Natural Sciences Education*, vol. 32, no. 5, pp. 42–48, 2017.

[56] Y. Zhu, Y. Wang, S. Chen, H. Zhang, and C. Fu, "Qualitative-quantitative multiscale characterization of pore structures in shale reservoirs: a case study of Longmaxi formation in the upper Yangtze area," *Earth Science Frontiers*, vol. 23, no. 1, pp. 154–163, 2016.

[57] R. C. Surdam, L. J. Crossey, E. S. Hagen, and H. P. Heasler, "Organic-inorganic interactions and sandstone diagenesis," *AAPG Bulletin*, vol. 73, no. 1, pp. 1–23, 1989.

[58] H. Dehghanpour, H. Zubair, A. Chhabra, and A. Ullah, "Liquid intake of organic shales," *Energy & Fuels*, vol. 26, no. 9, pp. 5750–5758, 2012.

[59] Q. Lan, H. Dehghanpour, J. Wood, and H. Sanei, "Wettability of the Montney tight gas formation," *SPE Reservoir Evaluation and Engineering*, vol. 18, no. 3, pp. 417–431, 2015.

[60] L. Handy, "Determination of effective capillary pressures for porous media from imbibition data," *Transactions of AIME*, vol. 219, no. 1, pp. 75–80, 1960.

[61] Q. H. Hu, W. Zhou, P. Huggins, and W. L. Chen, "Pore structure and fluid uptake of the Goddard shale formation in Southeastern Oklahoma," *Geofluids*, vol. 2018, Article ID 5381735, 16 pages, 2018.

[62] R. Yang, Q. Hu, S. He et al., "Pore structure, wettability and tracer migration in four leading shale formations in the middle Yangtze platform, China," *Marine and Petroleum Geology*, vol. 89, no. 2, pp. 415–427, 2018.

[63] M. E. Curtis, B. J. Cardott, C. H. Sondergeld, and C. S. Rai, "Development of organic porosity in the Woodford shale with increasing thermal maturity," *International Journal of Coal Geology*, vol. 103, no. 12, pp. 26–31, 2012.

[64] M. G. Kibria, Q. H. Hu, H. Liu, Y. X. Zhang, and J. H. Kang, "Pore structure, wettability, and spontaneous imbibition of Woodford shale, Permian Basin, West Texas," *Marine and Petroleum Geology*, vol. 91, pp. 735–748, 2018.

[65] L. F. Ruppert, R. Sakurovs, T. P. Blach et al., "A USANS/SANS study of the accessibility of pores in the Barnett shale to methane and water," *Energy & Fuels*, vol. 27, no. 2, pp. 772–779, 2013.

[66] M. Sun, B. Yu, Q. Hu, R. Yang, Y. Zhang, and B. Li, "Pore connectivity and tracer migration of typical shales in South China," *Fuel*, vol. 203, pp. 32–46, 2017.

[67] R. Yang, X. S. Guo, J. Z. Yi, Z. G. Shu, Q. H. Hu, and S. He, "Spontaneous imbibition of three leading shale formations in the middle Yangtze platform, South China," *Energy Fuels*, vol. 31, no. 7, pp. 6903–6916, 2017.

[68] S. Y. Yang, H. G. Qiao, B. Chen, and Q. H. Hu, "Solvent extraction efficiency of an Eocene-aged organic-rich lacustrine shale," *Marine and Petroleum Geology*, vol. 126, article 104941, 2021.